Supplementary Information for

Unlocking the potential of V_2O_5 decorated on crossed g-C_3N_4 monolayers derived from synergistic bio-transformation of $ZnMn_2O_4$ for antibiotic photodegradation

Ashkan Bahadoran[a], Nene Ajinkya[a], Mohammadreza Sharghi[b], Farzad Hasanvandian[c], Yan Wang[d], Huiwen Chen[e], Mina Namvari[f], Babak Kakavandi[g,h,*], Enrico Marsili[i], Massimiliano Galluzzi[a,*], Seeram Rama Krishna[j,*]

[a] Laboratory of Inflammation and Vaccines, Shenzhen Institute of Advanced Technology, Chinese Academy of Sciences, Shenzhen 518071, China

[b] Department of Chemistry, Binghamton University, The State University of New York, 4400 Vestal Parkway East, Binghamton, NY, 13902, United States

[c] Department of Chemical and Petroleum Engineering, Sharif University of Technology, Tehran, Iran

[d] Institute of Advanced Materials Science and Engineering, Shenzhen Institute of Advanced Technology, Chinese Academy of Sciences, Shenzhen 518055, Guangdong, China

[e] Materials Interfaces Center, Shenzhen Institute of Advanced Technology, Chinese Academy of Sciences, Shenzhen, Guangdong, 518055, China

[f] Sabanci University Nanotechnology Research and Application Center (SUNUM), Sabanci University, 34956, Istanbul, Turkey

[g] Research Center for Health, Safety, and Environment, Alborz University of Medical Sciences, Karaj, Iran

[h] Department of Environmental Health Engineering, Alborz University of Medical Sciences, Karaj, Iran

[i] Nottingham Ningbo China Beacons of Excellence Research and Innovation Institute, University of Nottingham Ningbo China, Ningbo, China

[j] NUS Center for Nanofibers and Nanotechnology, Department of Mechanical Engineering, National University of Singapore, Singapore

---

[*] **Corresponding authors at:**

Department of Environmental Health Engineering, Alborz University of Medical Sciences, Karaj, Iran. E-mail address: kakavandibvch@gmail.com (B. Kakavandi).

Laboratory of Inflammation and Vaccines, Shenzhen Institute of Advanced Technology, Chinese Academy of Sciences, Shenzhen 518071, China. E-mail address: galluzzi@siat.ac.cn (M. Galluzzi).

NUS Center for Nanofibers and Nanotechnology, Department of Mechanical Engineering, National University of Singapore, Singapore. E-mail address: seeram@nus.edu.sg (S. Ramakrishna).

1. Experimental

1.1. Chemicals and solvents

All the analytical grade chemicals and reagents were purchased from Mark Company (Darmstadt, Germany) and used as received, unless otherwise mentioned. Particularly, melamine ($C_3H_6N_6$) was used as the precursor of g-C_3N_4, while ammonium vanadate (NH_4VO_3) was used as a vanadium source. To fabricate the bio-synthetic (X)ZM nanoparticles, manganese nitrate ($Mn(NO_3)_2{\cdot}6H_2O$) and zinc nitrate ($Zn(NO_3)_2{\cdot}6H_2O$) were used as precursors of the Mn and Zn, and the aloe vera (AV) leaves (purchased from local market) were used as reducing agent. The antibiotic levofloxacin (LFC) was purchased from Sigma-Aldrich (USA). The other reagents used in the photocatalytic experiments were silver nitrate ($AgNO_3$), p-benzoquinone ($C_6H_4O_2$) [denoted as BQ], 2-propanol (C_3H_8O) [denoted as IPA], and disodium ethylenediaminetetraacetic acid ($C_{10}H_{16}N_2O_8$) [denoted as EDTA-Na] as the electrons (e^-), superoxide radicals ($O_2^{\bullet-}$), holes (h^+), and hydroxyl radicals ($HO^\bullet$) scavengers, respectively. The sodium hydroxide (NaOH) and hydrochloric acid (HCl 37%) were used to adjust the pH value. All the experiments were carried out in de-ionized water unless differently stated.

1.2. Preparation of AV solution

The AV leaves were cleaned with ultrapure water to remove dust and particle impurities. The green rind part of the leaves was cut to extract only the inner gel, which was then blended to form a colloidal solution (AV gel). The AV gel was mixed with ultrapure water in the proportion 40:60, 60:40, and 80:20 (w/w) to prepare the solutions A, B, and C, respectively, under vigorous stirring and at 70 ºC, until the solution became transparent. After that, the solutions were kept at 4 ºC until used.

1.3. Nanostructure characterization method

1.3.1. Instruments characterization

The investigation of the crystallographic features of the synthesized nanostructures was conducted through X-ray diffraction (XRD) (PANalytical XPert Pro MPD, Netherland), under CuKα irradiation, λ = 0.15406 nm, 40 kV, and 30 mA. The functional groups were characterized through Fourier transform infrared (FT-IR) spectroscopy (AVATAR, Thermo, USA). The morphological properties of the nanostructures were investigated through field emission scanning electron microscopy (FE-SEM) (Mira III, Tescan, Czech Republic) and transmission electron microscopy (TEM) (CM300, PHILIPS, Netherlands). The texture and porosity of the nanostructures were studied through N_2-gas ab-/de-sorption isotherms recorded through BELSORP MINI II, BEL, Japan. The optical feature of the nanostructures was characterized through UV-Vis diffuse reflectance spectroscopy (UV-Vis DRS) (Avaspec-2048-TEC spectrophotometer, Avantes, Netherland) and by steady state and time-resolved photoluminescence spectroscopy (PL) (Varian Cary Eclipse, Agilent, USA).

1.3.2. XPS characterization

The surface electronic traits were investigated by X-ray photoelectron spectroscopy (XPS) (K-alpha XPS spectrometer, Bes Tec, Germany), utilizing the MgKα radiation with 1253.6 eV X-ray as the excitation source. The XPS instrument was calibrated with the International Standards Organization (Document No. ISO 15472:2010: Surface chemical analysis, X-ray photoelectron spectrometers, Calibration of energy scales) through Au $4f_{7/2}$ of pure gold, while the Cu $2p_{3/2}$ and Cu 3p were utilized for separation in calibration energies. Owing to the intrinsic behaviors of semiconductors towards static charge, binding energy for each characteristic peak is expected to show higher energy for a few electron volts. The obtain this uncertainty, the value of retardation was determined by carbon adventitious (C 1s) evaluation, known as “charge referencing”. Because carbon adventitious exists in all experimental samples, this method is useable for all materials. Thus far, relatively a broad range has been suggested for the carbon adventitious

from 284.6 to 285.2 eV. However, the most reported value is 284.8 eV which is in line with Wagner's ref. at 1980 and Swift's ref. at 1982 [1,2]. Additionally, recently several experiments were conducted which confirmed the accuracy of this value [3]. Therefore, in this study, 284.8 eV was selected for the characterization of carbon adventitious and corresponding retardation values for which samples were illustrated in Fig. S1.

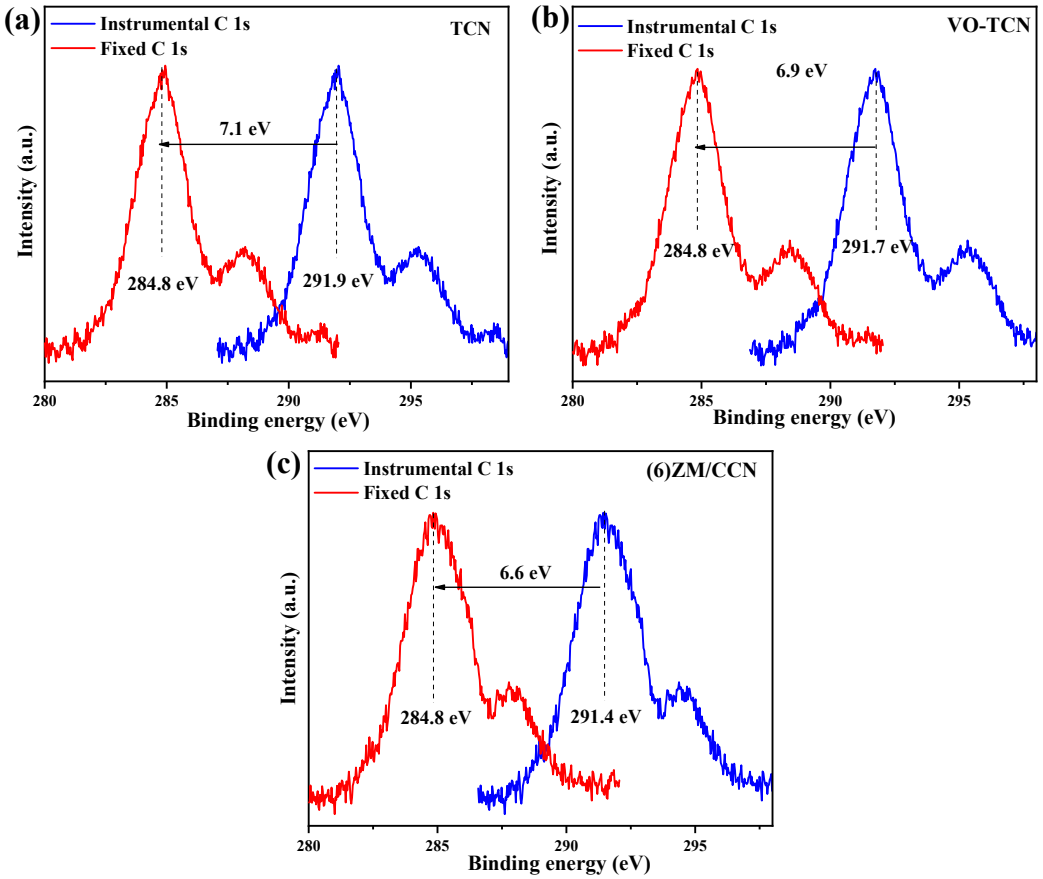

Fig. S1. retardation peak of C 1s spectra for various samples.

1.3.3. Procedure of photoelectrochemical characterization

The photoelectrochemical properties of the nanostructures were characterized by transient photocurrent (TP), electrochemical impedance spectroscopy (EIS), and Mott-Schottky (MS) analyses, which were conducted with PalmSens4 potentiostat equipped with three-electrode arrangement, including Pt wire as

a counter electrode, Ag/AgCl reference electrode, and glassy carbon electrode as a working electrode. Additionally, the acquired potentials versus Ag/AgCl were converted to normal hydrogen electrodes using Eq. S1.

$$E(NHE) = E(Ag/AgCl) + 0.197V. \quad (S1)$$

The EIS and MS analyses were operated at 0.5 M of Na_2SO_4 solution as an electrolyte media, while the working electrode was a catalyst-coated glassy carbon electrode (C-GCE). For EIS, the voltage of the instrument was fixed at open circuit potential and frequency varied from 100 kHz to 0.01 Hz. For MS, the signal was traced at three fixed frequencies, including 0.5, 1, and 1.5 kHz. The TP analysis was apprised in a media that was comprised of 0.1 M K_2SO_4, 0.05 M KH_2PO_4, and 0.05 M NaH_2PO_4. When the working electrode was subjected to irradiation of Xe lamp (300 W) with 50 second on and off situation, the current was measured where the potential ranged from -1 to 0 V (versus Ag/AgCl) with a sweep rate of 20 mV. Furthermore, the working electrode was a catalyst-coated fluorine-doped tin oxide (C-FTO).

In the matter of using C-GCE and C-FTO, the preparation procedures were as follows:

A solution containing 385 µL of DI water, 100 µL of isopropanol, and 15 µL of D521 Nafion solution (5 wt.%) was prepared, and then 2.5 mg of as-synthesized catalyst was added. The obtained contain was kept under sonication for 30 min until well-homogenous suspension appeared. In the case of C-GCE, 1 µL of prepared suspension was applied on a glassy carbon electrode with 2.0 mm in diameter using the drop-casting method. In the case of C-FTO, a certain volume of prepared suspension was loaded on FTO using the drop-casting method so that catalyst loading was 1 mg/cm^2. After C-FTO was naturally dried in ambient conditions, it was transferred for calcination at 300 ºC for 2 h.

1.4. Photodegradation reaction setup

The photocatalytic activity of the nanostructures was tested over LFC photodegradation in a double-shell cylindrical pyrex vessel and 300 mL capacity (Fig. S2), maintained at 25 ºC with a water jacket. The photoreactor was exposed to a 300 W Xe lamp with the light spectrum shown in Fig. S3, equipped with a cut-off filter and set at the top of the photoreactor. The light irradiation produced ~100 mW/cm^2 of the light intensity. 200 mL of solution containing a specific LFC concentration was poured into the reactor, and then the pH of the media was fixed at the desired value using HCl 0.1 M or NaOH 0.1 M. The nanostructures were dispersed into the reaction media with a magnetic stirrer. Before the photocatalytic reaction, the photoreactor was kept in the dark to equilibrate the adsorption/desorption of the LFC to the nanostructures. After the equilibration step, the lamp was turned on. The progress of the photodegradation process was monitored at 20 min intervals when 5 mL of solution was withdrawn. The liquid phase was separated from the solid phase catalyst through centrifugation. The supernatant was then transferred to the UV–vis spectrophotometer (Unico 4802, Dayton, USA) to measure the light absorbance degree at λ_{max} (284 nm), which corresponds to the specific absorption peak of LFC. The progress of the photodegradation process was calculated through Eq. S2, where C_i and Cr correspond to the initial and residual LFC concentration.

$$Photodegradation\ rate\ (\%) = \left(\frac{C_i - C_r}{C_i}\right) \times 10($$ (S2)

$$Mineralization\ rate\ (\%) = \left(\frac{TOC_i - TOC_r}{TOC_i}\right) \times 1$$ (S3)

$$AOS = 4 - 1.5 \times \left(\frac{COD_r}{TOC_r}\right)$$ (S4)

$$COS = 4 - 1.5 \times \left(\frac{COD_r}{TOC_i}\right)$$ (S5)

With total organic carbon (TOC), chemical oxygen demand (COD), carbon oxidation state (COS), and average oxidation state (AOS), where the subscript letters i and r correspond to the initial and residual value of each parameter.

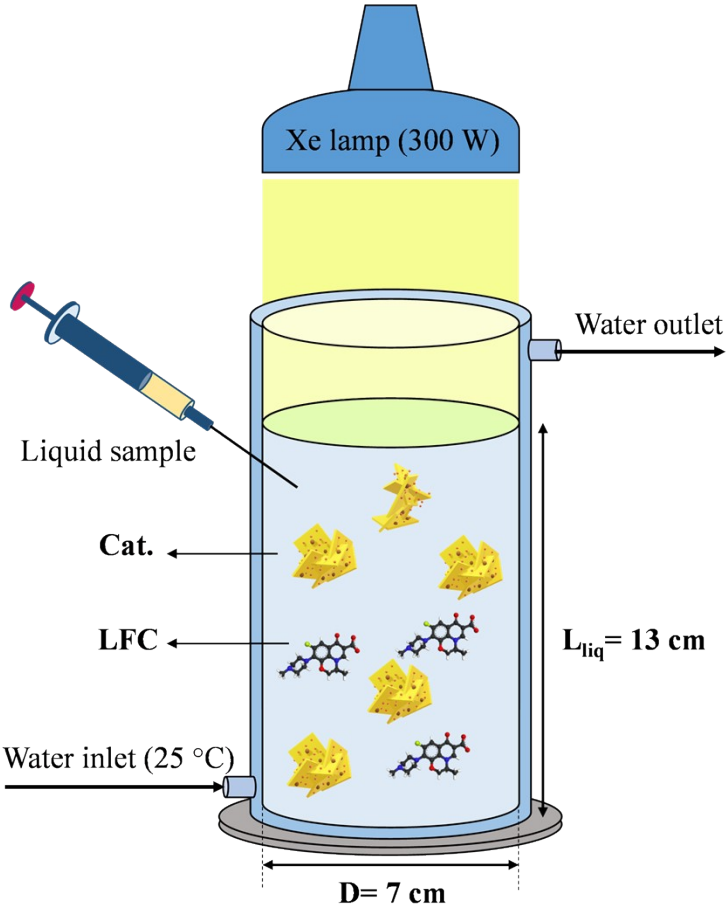

Fig. S2. Schematic of the 300 mL photoreactor used for LFC degradation

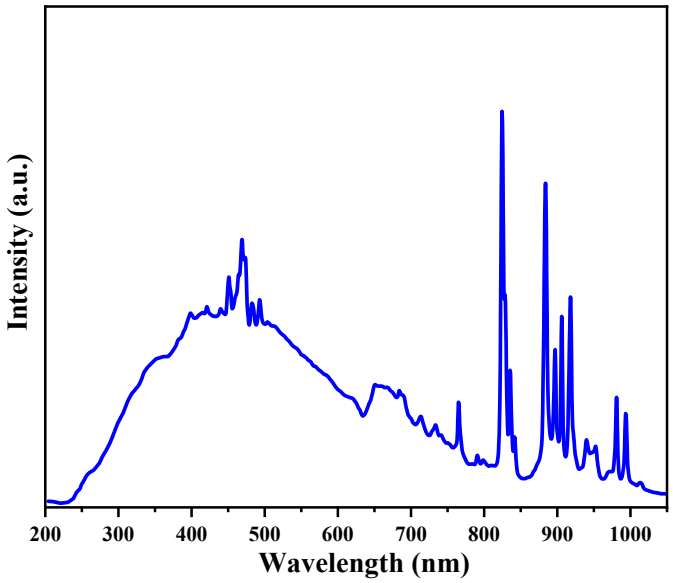

Fig. S3. Spectrum of Xe lamp (300 W)

2. Calculation

2.1. Scherrer formula

$$D = \frac{K \times \lambda}{\beta \times cos(\theta)} \quad \text{(S6)}$$

Where, D: crystalline size (nm), K: Shape factor, λ: wavelength of the X-ray, β: width of the diffraction peak, θ: diffraction angle,

2.2. S_{BET}

Eq. S7 is commonly used for the calculation of S_{BET}:

$$\frac{\frac{P}{P_{atm}}}{V\left[1-(\frac{P}{P_{atm}})\right]} = \frac{1}{V_{monolayer}} + \frac{C-1}{V_{monolayer}} \frac{P}{P_{atm}} \quad \text{(S7)}$$

Eq. S7 is usually linear over the relative pressure range of 0.05-0.35. Besides, “a” and “b” are the slope and intercept of the linear function. Thus, Eq. S8 is defined for the calculation of S_{BET}, where a is the cross-section area of the N_2 molecule and N_A is the Avogadro constant.

$$S_{BET} = \frac{a \times N_A}{(a+b) \times V_{monolayer}} \quad \text{(S8)}$$

In addition, Eq. S9 is defined for estimating the uncertainty value of reported S_{BET}.

$$the\ the\ u_c(y) = \sqrt{[u_c(y)]^2} = \sqrt{\frac{1}{n-2}\sum_{i=1}^{n}(y_i - a - bx_i)^2} \quad \text{(S9)}$$

2.3. E_g

The correct procedure consists of plotting the $(\alpha hv)^{n/2}$ versus (hv) and then fitting a linear portion of this curve by a straight line, in which the intercept divided by the slope provides the numerical value for E_g (Table 1).

The uncertainties that have been calculated from the linear fit parameters in Table 1 were determined through error propagation calculations using the quotient rule (Eq. S10).

$$u_c(y) = \sqrt{[u_c(y)]^2} = \sqrt{\frac{1}{n-2}\sum_{i=1}^{n}(y_i - a - bx_i)^2} \quad \text{(S10)}$$

Where, "a" and "b" are the slope and intercept of the linear function, while y is the real diffuse-reflectance values.

2.4. The bi-exponential function of time-resolved PL

$$I(t) = A_1\, exp(-\frac{t}{T_1}) + A_2\, exp(-\frac{t}{T_2}) \quad \text{(S11)}$$

$$\tau_{ave.} = \frac{A_1 T_1^2 + A_2 T_2^2}{A_1 T_1 + A_2 T_2} \quad \text{(S12)}$$

The uncertainty value for each sample has now been calculated based on the following equation:

$$u_c(I) = \sqrt{[u_c(I)]^2} = \sqrt{\frac{1}{n-2}\sum_{i=1}^{n}(I_i - A_1\, exp(-\frac{t}{T_1}) - A_2\, exp(-\frac{t}{T_2}))^2} \quad \text{(S13)}$$

2.5. Photodegradation data

$$u_c(I) = \sqrt{[u_c(y)]^2} = \sqrt{\frac{1}{n-2}\sum_{i=1}^{n}(y_i - ln(\frac{C_i}{C_t}))^2} \quad \text{(S14)}$$

The photocatalysis process in the presence of all tested nanostructures was represented by the modified Langmuir–Hinshelwood (LH) kinetic model. Thus, the uncertainty value of each catalyst with the LH model can be calculated by Eq. S14.

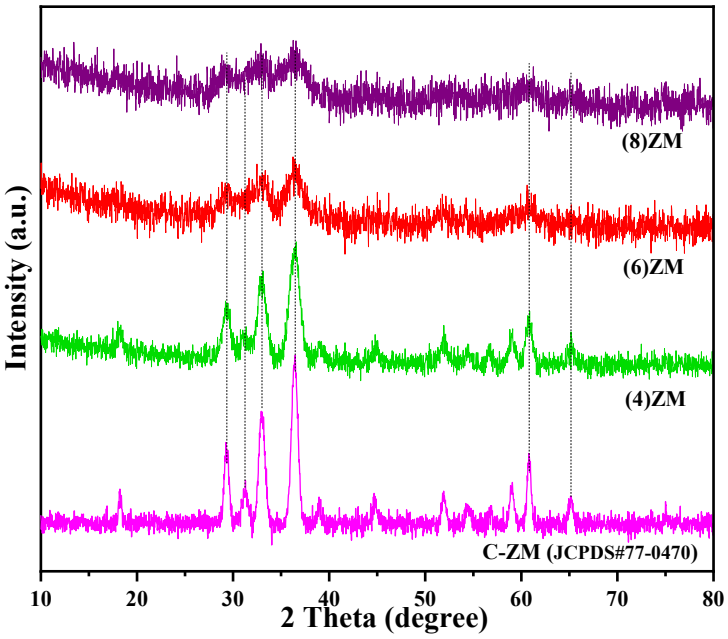

Fig. S4. The XRD patterns of all (X)ZM and (C)ZM nanomaterials.

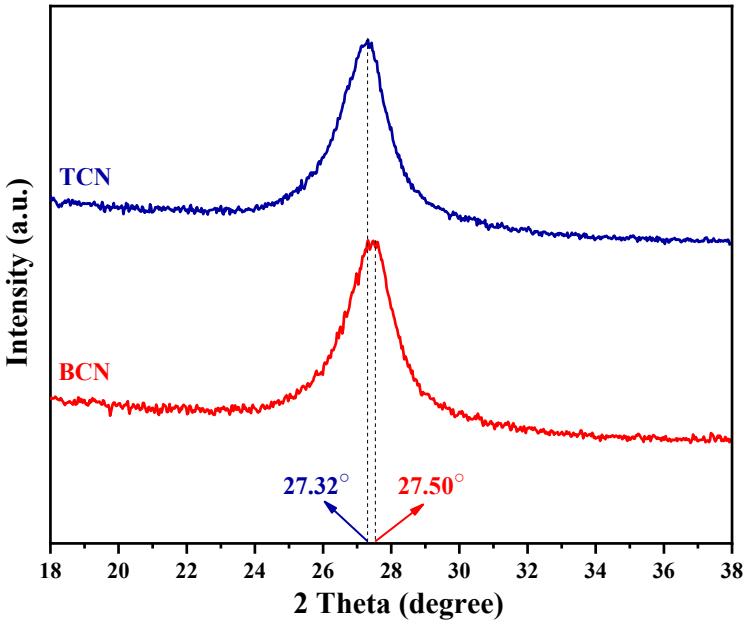

Fig. S5. The comparison of the XRD spectra of BCN and TCN

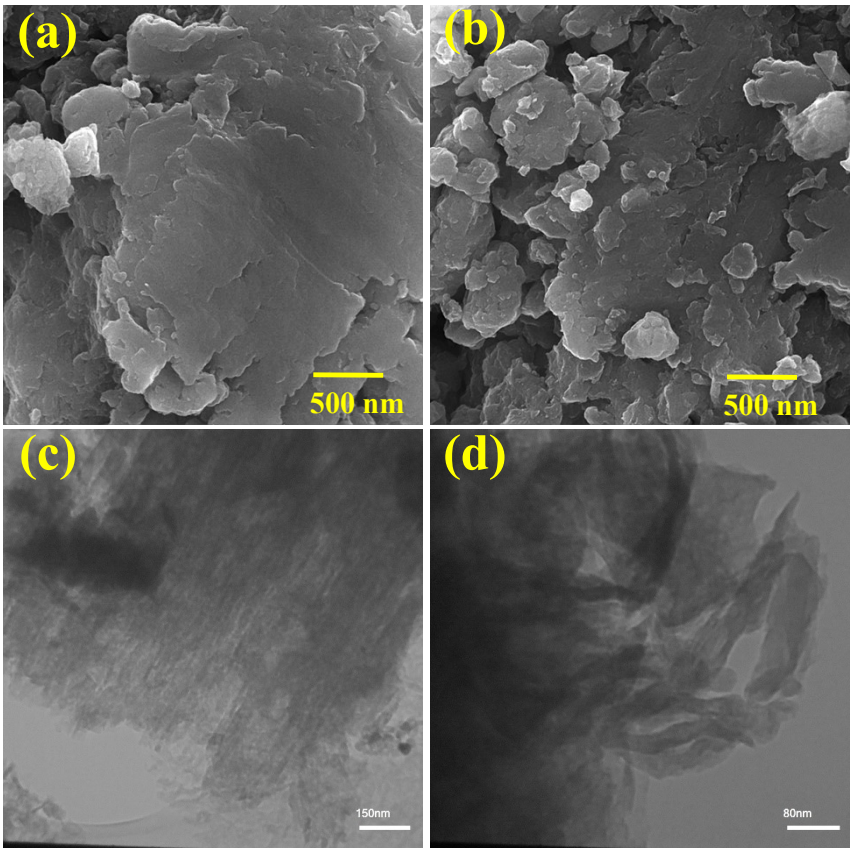

Fig. S6. The SE-FEM images of (a) BCN, (b) TCN, the TEM photographs of (c) BCN, and (d) TCN

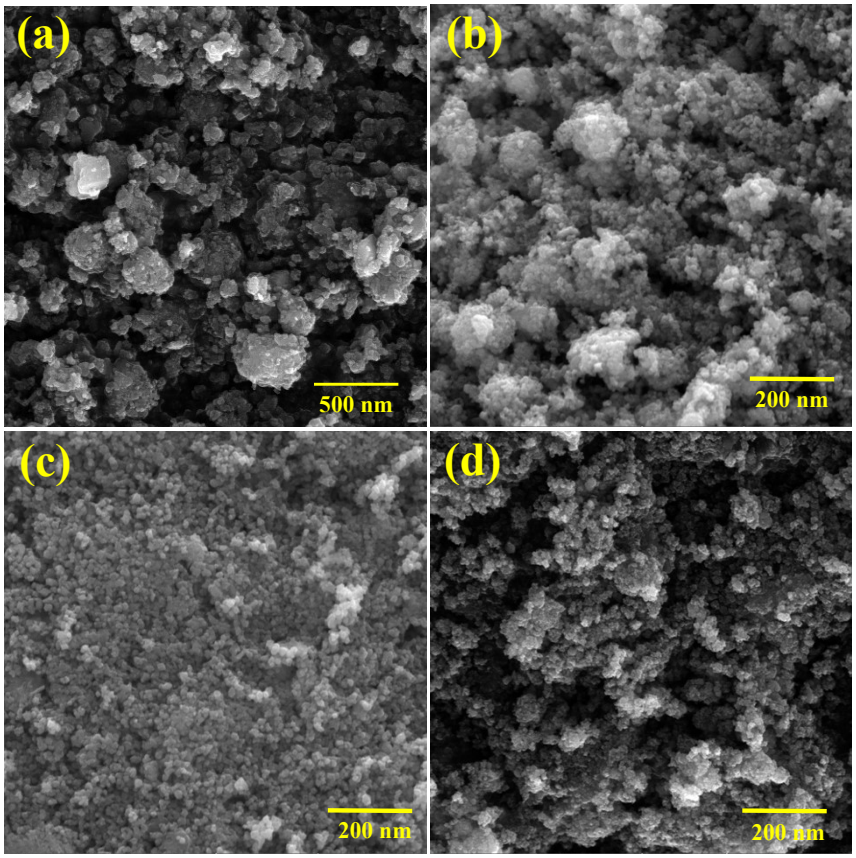

Fig. S7. The FE-SEM images of (a) (C)ZM, (b) (4)ZM, (c) (6)ZM, and (d) (8)ZM samples

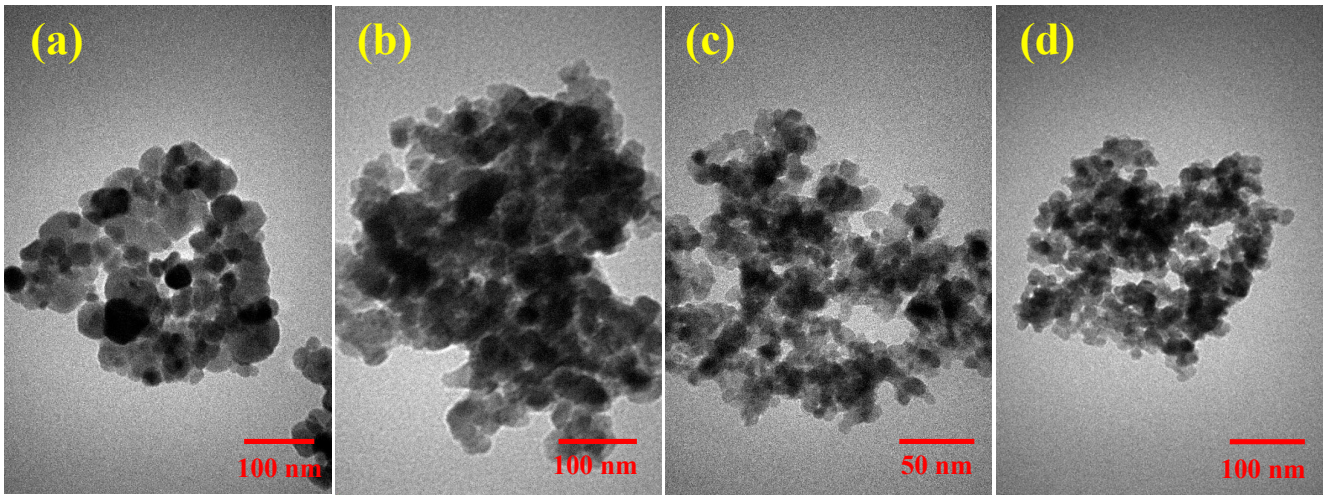

Fig. S8. The TEM photographs of (a) (C)ZM, (b) (4)ZM, (c) (6)ZM, and (d) (8)ZM nanoparticles

Fig. S9. Size distribution of nanoparticles (a) (4)ZM, (b) (6)ZM, and (c) (8)ZM nanoparticles

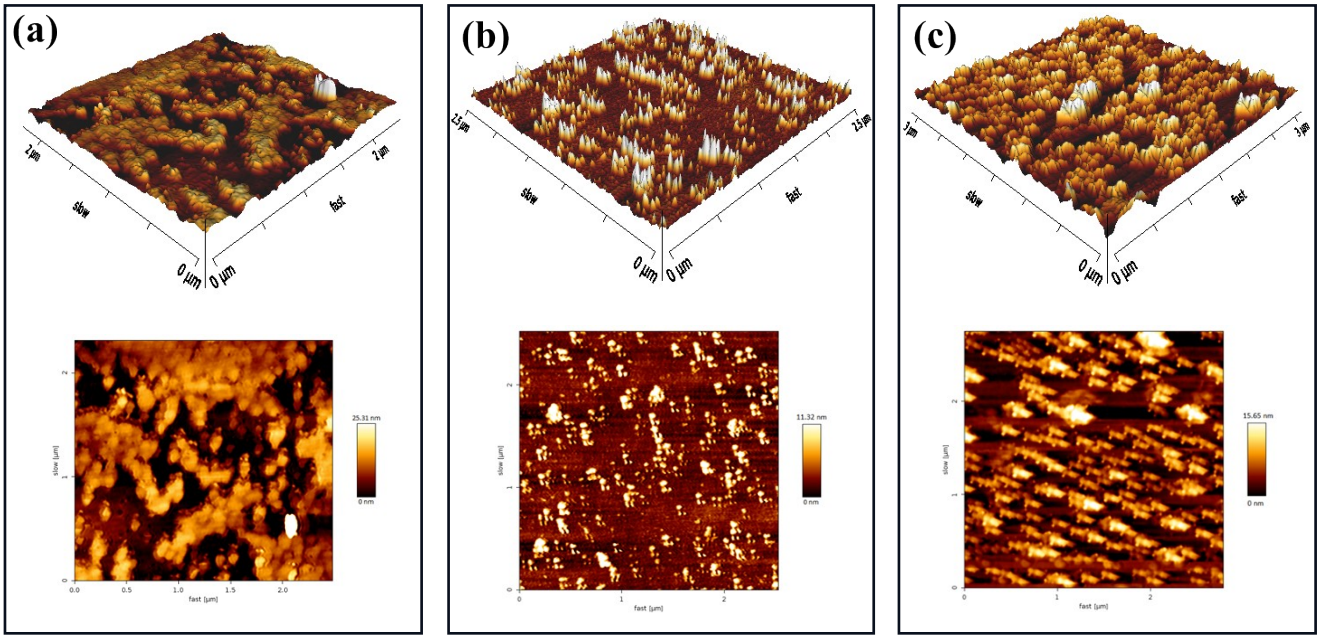

Fig. S10. The AFM analysis related to (a) (4)ZM, (b) (6)ZM, and (c) (8)ZM samples.

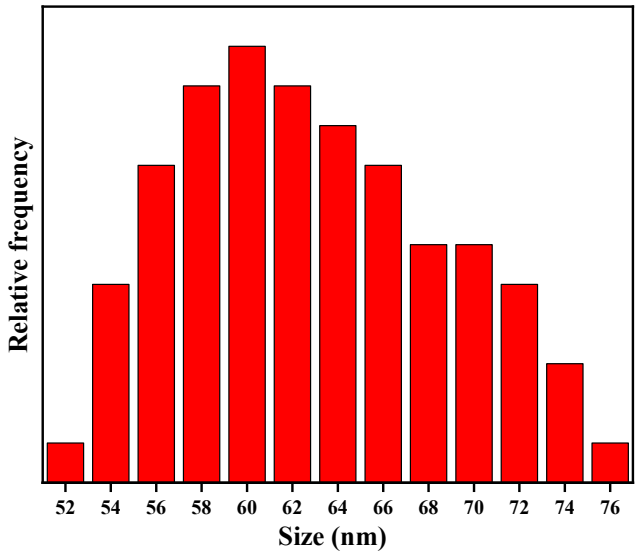

Fig. S11. The size distribution of VO nanoparticles

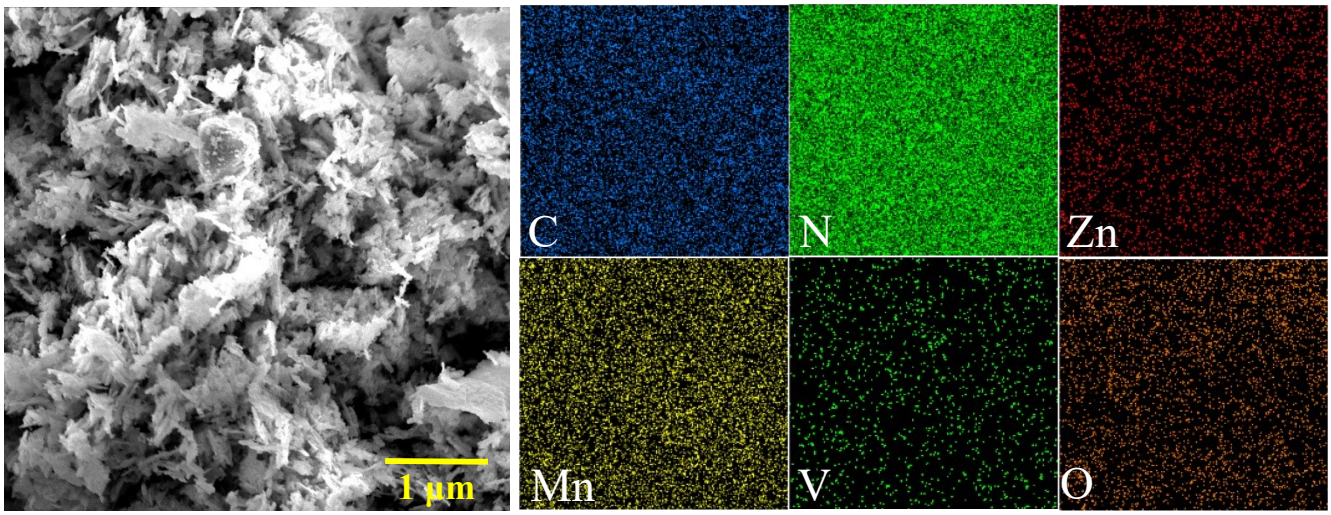

Fig. S12. The elemental mapping of ternary VO-(6)ZM/CCN nanostructure.

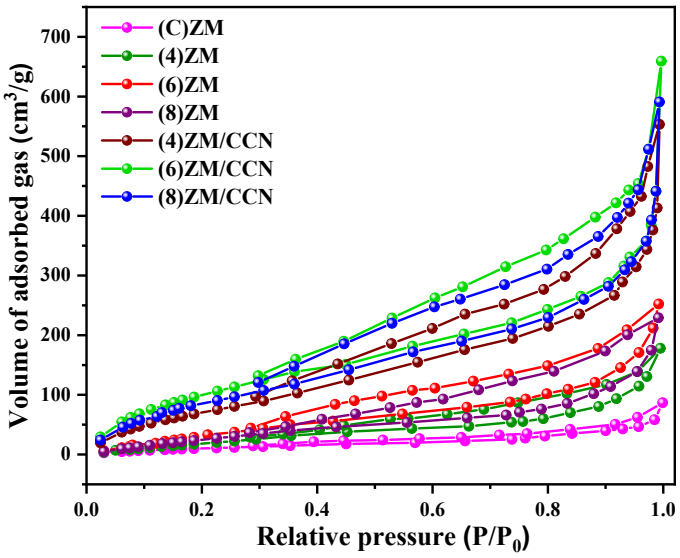

Fig. S13. N_2-gas ad/desorption isotherms of (C)ZM, (X)ZM, and (X)ZM/CCN

Fig. S14. (a) The DRS plots and (b) Tauc plots attributed to (C)ZM and (X)ZM samples

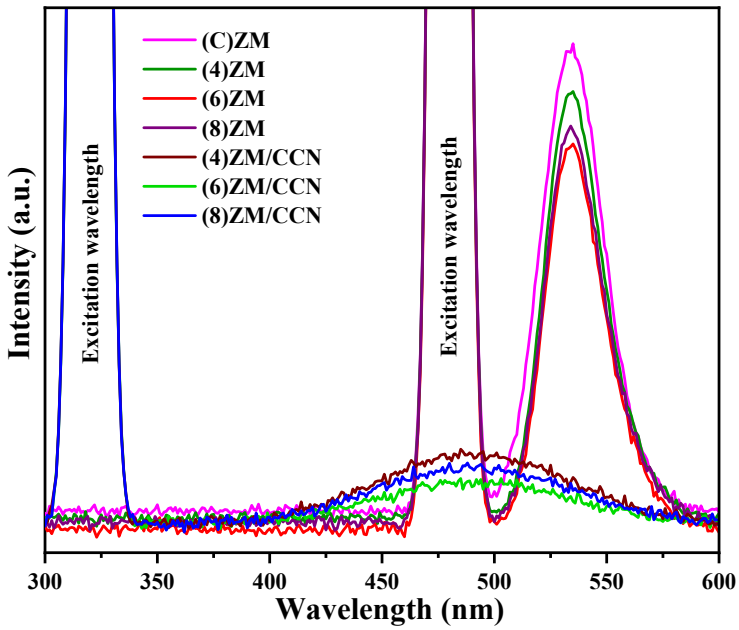

Fig. S15. The steady-state PL response of (C)ZM, (X)ZM, and (X)ZM/CCN

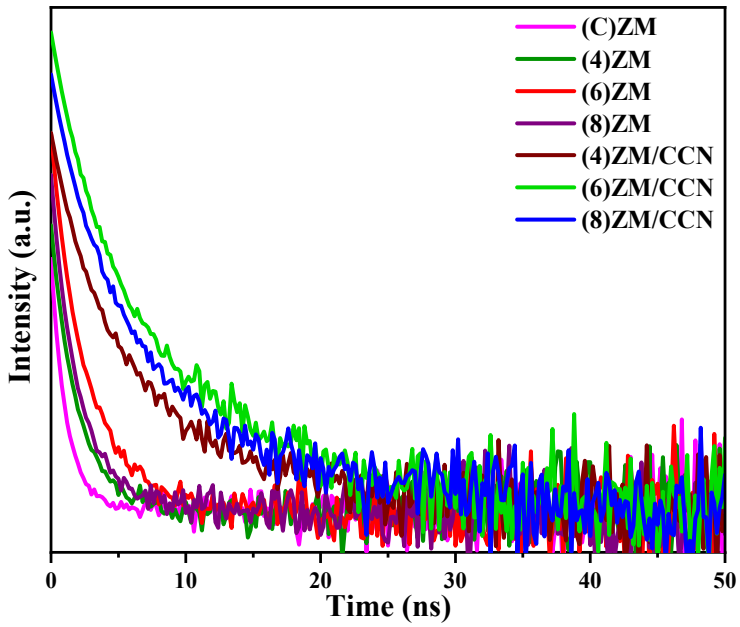

Fig. S16. The time-resolved PL response of (C)ZM, (X)ZM, and (X)ZM/CCN

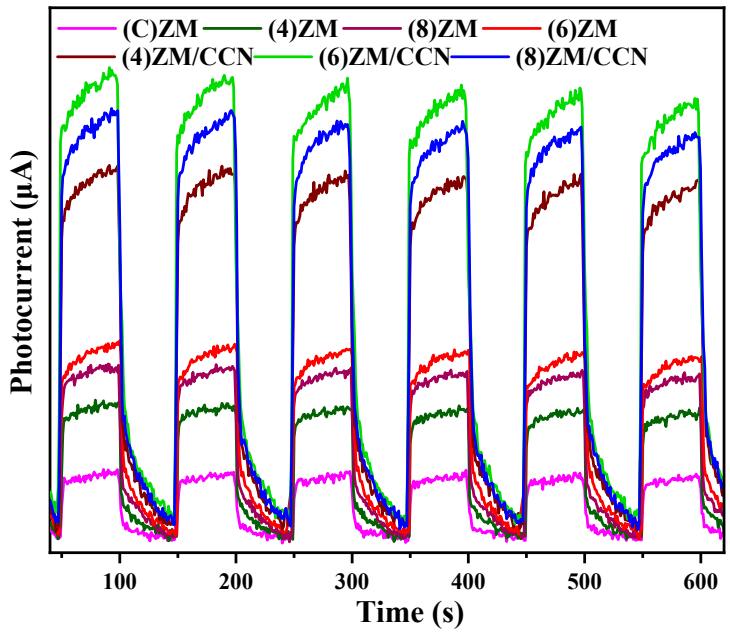

Fig. S17. The TP response of the (C)ZM, (X)ZM, and (X)ZM/CCN

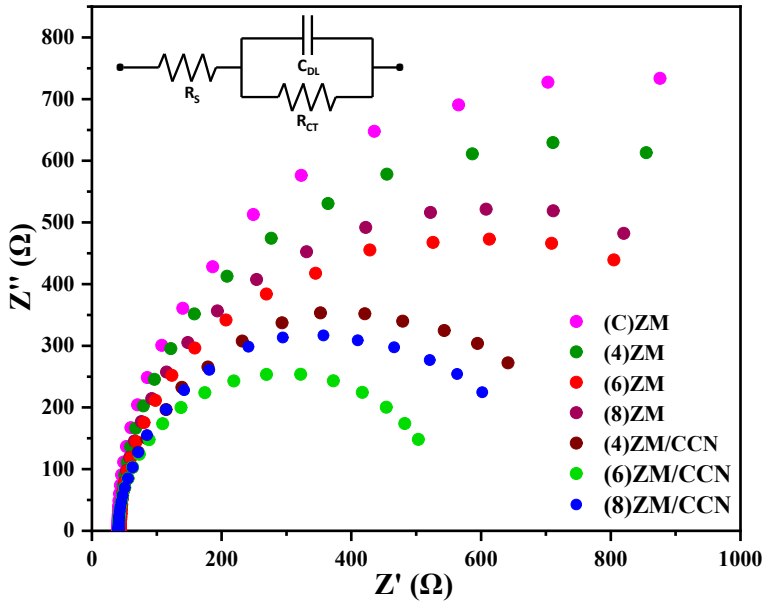

Fig. S18. The EIS response of the (C)ZM, (X)ZM, and (X)ZM/CCN

Fig. S19. (a) The photodegradation performance of diverse as-synthesized (C)ZM, (X)ZM, and (X)ZM/CCN under optimal reaction variables (primeval-pH: 6, nanomaterial loading: 0.9 g/L, and LFC concentration: 50 mg/L), (b) fitting LH pseudo-first-order kinetic model with LFC decontamination output of as-fabricated

(C)ZM, (X)ZM, and (X)ZM/CCN catalysts under optimized operational conditions, (c) kinetic insight over the photocatalytic LFC disintegration

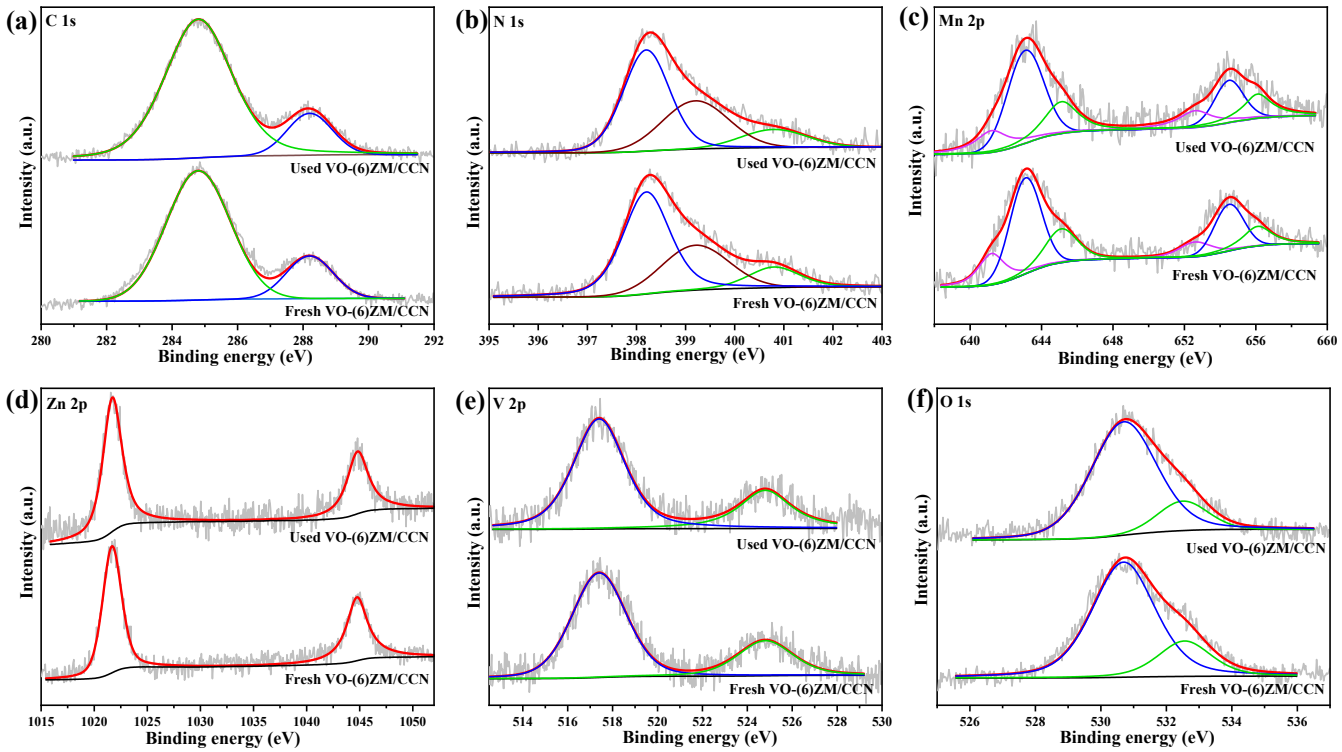

Fig. S20. The HR-XPS patterns of VO-(6)ZM/CCN nanocomposite prior and post to six successive runs of LFC photodisintegration.

3. Scrutinization of charge carrier mechanism

The as-derived $E_{fb}|_{NHE}$ values of C-ZM, (4)ZM, (6)ZM, and (8)ZM were estimated to be 0.33, 0.36, 0.41, and 0.42 V, respectively. By supposing that E_{VB} values of the p-type X-ZM samples were located approximately 0.1 eV lower than their corresponding E_{fb} values, $E_{VB}|_{(C)ZM}=0.43$ V, $E_{VB}|_{(4)ZM}=0.46$ V, $E_{VB}|_{(6)ZM}=0.51$ V, and $E_{VB}|_{(8)ZM}=0.52$ V were achieved, which were comparable to their related VB-XPS outcomes. In addition, the E_{CB} values were calculated to be $E_{CB}|_{(C)ZM}=-1.43$ V, $E_{CB}|_{(4)ZM}=-1.66$ V, $E_{CB}|_{(6)ZM}=-1.73$ V, and $E_{CB}|_{(8)ZM}=-1.74$ V. The increased redox potential was rooted in the quantum confinement effect originating from the systematic reduction in particle size [4,5].

Fig. S21. The MS plots and VB-XPS curves of (a and a_1) (C)ZM, (b and b_1) (4)ZM, (c and c_1) (6)ZM, (d and d_1), and (e) the band edge structure of (C)ZM and (X)ZM.

The carrier density ($N_{(x = d \text{ or } a)}$), where N_d represents the donor density for n-type materials and N_a represents the acceptor density for p-type materials, is the basis of the charge transfer principle and promotion of photochemical properties. The carrier density was derived from MS equations (Eq. S15), emphasizing that carrier density increased in inverse proportion to the slope of MS plots [6].

$$the\ N_D = \frac{2}{e\ \varepsilon_0\ \varepsilon_r}\left(\frac{dE}{dC^2}\right) = \frac{2}{e\ \varepsilon_0\ \varepsilon_r}\left(\frac{1}{slope}\right) \quad \text{(S15)}$$

According to Fig 8(c), the negatively shifted $E_{fb}\big|_{TCN}$ demonstrated the expanding band edge position of TCN resulting from thermally exfoliated g-C_3N_4, compared to the BCN sample. Moreover, in comparison with BCN, the corresponding MS slope of TCN decreased, suggesting improved photoelectrochemical features. When biosynthesized (6)ZM nanoparticles engaged in CCN monolayers, the slope of the MS plot decreased, highlighting the photocatalytic capability of the heterogeneous Z-schematic (6)ZM/CCN system. Notably, $E_{fb}\big|_{(6)ZM/CCN}$ exhibited a negative shift of 130 mV compared with pristine TCN due to the changed onset potential of the (6)ZM/CCN electrode resulting from the decreased Fermi level of the related carbon nitride [7,8]. Additionally, after the amalgamation of VO

nanoparticles with the binary system, improved carrier density and a perceptible negative shift in E_{fb} (approximately 50 mV) were observed, confirming the favorable mutual electronic interaction of the final nanocomposite.

Fig. S22. The inhibitory effect of each quenching agents on LFC photodisintegration of (a) (6)ZM, (b) TCN, (c) VO, (d) (6)ZM/CCN, and (e) VO/TCN samples

Table S1. Comparison of the reported specific surface area attributed to $ZnMn_2O_4$ nanoparticles with the as-synthesized 6-ZMO in current research

Sample	**$S_{(BET)}$ (m^2/g)**	**V_p (cm^3/g)**	**Ref.**
$ZnMn_2O_4$ nanoparticles	19.1	-	[9]
$ZnMn_2O_4$ nanoparticles	23.9	0.10	[10]
$ZnMn_2O_4$ nanoparticles	45.1	-	[11]
$ZnMn_2O_4$ nanoparticles	45.9	-	[12]
$ZnMn_2O_4$ nanoparticles	67.0	0.13	[13]
MOF-driven $ZnMn_2O_4$ nanoparticles	109.1	0.31	[14]
(6)ZM	**128**	**0.91**	**This study**

Table S2. The fitted parameters of time-resolved PL attributed to different materials extracted from fitting with bi-exponential function.

sample	**A_1**	**T_1**	**A_2**	**T_2**	**$T_2A_2/(T_1A_1 + T_2A_2)$ (%)**	**$T_{ave.}$ (ns)**
VO	16	1.9	23	2.6	66	2.36

TCN	14	1.7	20	2.2	64	2.02
(C)ZM	13	1.4	17	1	48	1.20
(4)ZM	15	1.6	19	2.3	64	2.05
(6)ZM	19	1.7	26	3.5	74	3.03
(8)ZM	21	1.5	19	2.8	63	2.31
VO/TCN	25	2.3	22	6.3	70	5.12
(4)ZM/CNN	17	2.9	28	9.6	84	8.56
(6)ZM/CCN	21	3.3	36	11.4	86	10.23
(8)ZM/CCN	19	3.2	33	10.6	85	9.50
VO-(6)ZM/CCN	28	3.6	48	14.6	87	13.21

Table S3. The systematic differentiation between the LFC detoxification capability of the unprecedently constructed system in THE current paper with other previously reported research in the literature.

Nanostructure system	**Catalyst loading (g/L)**	**LFC concentration (mg/L)**	**Light source**	**Light intensity (mW/cm^2)**	**Detoxification ratio (%)**	**Rate constant ($min^{-1}\times 10^3$)**	**Reaction time (min)**	**Ref.**
$CdS/g\text{-}C_3N_4$	0.4	5	LED lamp	-	66.0	4.6	200	15
$Au/Ni_2P/g\text{-}C_3N_4$	1	10	Xe lamp (300 W)	-	88.2	N. A	140	16
Z-scheme $CdS/Bi_{12}GeO_{20}$	0.5	10	Xe lamp (250 W)	150	80.0	N. A	120	17
Ag_3VO_4/Ag_2CO_3	0.5	10	Xe lamp (500 W)	95	82.0	26.4	60	18
$MoS_2/ZnSe$	0.3	11	Xe lamp (500 W)	100	73.2	8.7	120	19
$Sm_6WO_{12}/g\text{-}C_3N_4$	0.5	10	Tungsten lamp	150	90.8	34.0	70	20
ZnFe2O4/ $NCDs/Ag_2CO_3$	0.6	10	Xe lamp (300 W)	-	88.7	20.8	90	21
Ta_3N_5/TiO_2	1	10	Xe lamp (250 W)	-	92.7	18.6	120	22
$CeVO_4/BiVO_4$	0.5	50	Xe lamp (150 W)	-	95.7	-	300	23
$(BiOBr)_x$ $(Bi_7O_9I_3)_{1-x}$	1	50	halogen bulb (400 W)	-	95.4	28.4	120	24

Ag_2CO_3/CeO_2/ AgBr	0.5	10	Xe lamp (300 W)	-	87.0	-	40	[25]
BiCrO6/g-C3N4	0.9	15	LED (100W)	100	92	21.9	120	[26]
V_2O_5/g-$C_3N_4/CuCo_2O_4$	0.7	20	LED (100W)	100	95.0	24.9	120	[27]
V_2O_5/g-$C_3N_4/CuCo_2S_4$	0.7	25	LED (100W)	100	98.0	26.7	120	[28]
VO-(6)ZM/CCN	**0.9**	**50**	**Xe lamp (300 W)**	**100**	**98.0**	**32.1**	**120**	**This study**

Table S4. The characteristic parameters pertinent to the quality variable of real wastewater sample

Parameter	The range of variables	The mean value of the parameter
BOD_5 (mg/L)	107-149	128
Total COD (mg/L)	2050-2530	2290
BOD_5/COD	-	0.056
TOC (mg/L)	746-988	867
TDS (mg/L)	2459-2983	2721
Turbidity (NTU)	11-24	17.5
TSS (mg/L)	224-278	251
pH	6.5-8.4	7.45

Reference

1 R. J. Bird and P. Swift, *J. Electron Spectros. Relat. Phenomena*, 1980, **21**, 227–240.

2 P. Swift, *Surf. Interface Anal.*, 1982, **4**, 47–51.

3 B. V. Crist, *J. Electron Spectros. Relat. Phenomena*, 2019, **231**, 75–87.

4 Y. Zhang, Z. Huang, C.-L. Dong, J. Shi, C. Cheng, X. Guan, S. Zong, B. Luo, Z. Cheng and D. Wei, *Chem. Eng. J.*, 2022, **431**, 134101.

5 A. Li, T. Wang, C. Li, Z. Huang, Z. Luo and J. Gong, *Angew. Chemie Int. Ed.*, 2019, **58**, 3804–3808.

6 K. Bhunia, M. Chandra, S. Khilari and D. Pradhan, *ACS Appl. Mater. Interfaces*, 2018, **11**, 478–488.

7 F. Meng, S. K. Cushing, J. Li, S. Hao and N. Wu, *Acs Catal.*, 2015, **5**, 1949–1955.

8 T. Soltani, A. Tayyebi and B.-K. Lee, *Catal. Today*, 2020, **340**, 188–196.

9 Q. Ni, H. Cheng, J. Ma, Y. Kong and S. Komarneni, *Front. Chem. Sci. Eng.*, 2020, **14**, 956–966.

10 C. Chen, Y. Huang, Q. Fang and S. Wang, *J. Alloys Compd.*, 2021, **889**, 161654.

11 R. Gherbi, M. Benamira and Y. Bessekhouad, *J. Alloys Compd.*, 2021, **851**, 156797.

12 R. Gherbi, Y. Bessekhouad and M. Trari, *J. Alloys Compd.*, 2016, **655**, 188–197.

13 K. Aruchamy, R. Nagaraj, H. M. Manohara, M. R. Nidhi, D. Mondal, D. Ghosh and S. K. Nataraj, *Mater. Sci. Eng. B*, 2020, **252**, 114481.

14 S. Yan, Y. Yu and Y. Cao, *Appl. Surf. Sci.*, 2019, **465**, 383–388.

15 F. Al Marzouqi, Y. Kim and R. Selvaraj, *New J. Chem.*, 2019, **43**, 9784–9792.

16 Y. Q. He, F. Zhang, B. Ma, N. Xu, L. Binnah Junior, B. Yao, Q. Yang, D. Liu and Z. Ma, *Appl. Surf. Sci.*, 2020, **517**, 146187.

17 X. Ruan, H. Hu, H. Che, E. Jiang, X. Zhang, C. Liu and G. Che, *J. Colloid Interface Sci.*, 2019, **543**, 317–327.

18 H. Sun, P. Qin, Z. Wu, C. Liao, J. Guo, S. Luo and Y. Chai, *J. Alloys Compd.*, 2020, **834**, 155211.

19 E. Sitara, M. F. Ehsan, H. Nasir, S. Iram and S. A. B. Bukhari, *Catalysts*, 2020, **10**, 1–11.

20 S. L. Prabavathi, K. Saravanakumar, C. M. Park and V. Muthuraj, *Sep. Purif. Technol.*, 2021, **257**, 117985.

21 L. Li, C.-G. Niu, H. Guo, J. Wang, M. Ruan, L. Zhang, C. Liang, H.-Y. Liu and Y.-Y. Yang, *Chem. Eng. J.*, 2020, **383**, 123192.

22 Y. Jiang, X. Jing, K. Zhu, Z. Peng, J. Zhang, Y. Liu, W. Zhang, L. Ni and Z. Liu, *Dalt. Trans.*, 2018, **47**, 13113–13125.

23 G. Lu, Z. Lun, H. Liang, H. Wang, Z. Li and W. Ma, *J. Alloys Compd.*, 2019, **772**, 122–131.

24 S. G. Fard, M. Haghighi and M. Shabani, *Appl. Catal. B Environ.*, 2019, **248**, 320–331.

25 X.-J. Wen, C.-G. Niu, H. Guo, L. Zhang, C. Liang and G.-M. Zeng, *J. Catal.*, 2018, **358**, 211–223.

26 F. Hasanvandian, M. Moradi, S. A. Samani, B. Kakavandi, S. R. Setayesh and M. Noorisepehr, *Chemosphere*, 2022, **287**, 132273.

27 F. Hasanvandian, A. Shokri, M. Moradi, B. Kakavandi and S. R. Setayesh, *J. Hazard. Mater.*, 2022, **423**, 127090.

28 X. Yang, M. D. Hesami, E. Nazemipool, A. Bahadoran, M. Al-Bahrani and B. Azizi, *Sep. Purif. Technol.*, 2022, **301**, 122005.